(Preprint) AAS 25-115

ROBUST TRAJECTORY OPTIMIZATION FOR NRHO RENDEZVOUS USING SPICE KERNEL RELATIVE MOTION

David A. Cunningham[*], Ryan P. Russell[†], and David C. Woffinden[‡]

In this paper, robust optimization is performed on trajectory correction maneuvers during the lunar lander return phase of an Artemis mission, treating the trajectory from one hour after low lunar orbit departure to arrival in the vicinity of the lunar Gateway as a relative motion problem. To enable rapid stochastic optimization techniques requiring many candidate trajectories, SPICE kernel relative motion as implemented by the Quadratic Interpolated State Transition (QIST) system is used as the underlying dynamics propagation. The optimization is performed with a genetic optimizer using linear covariance (LinCov) software in a simplified operational context, taking into account the availability of navigation sensors with varying measurement models, ranges, and accuracies. No numerical integration is used, since the relative motion around Gateway is fully characterized with the a priori computation of the QIST coefficients. Maneuver placements are computed to optimize the minimum 3σ delta-v of the trajectory, the position dispersion at a target point, and a convex combination of these two metrics. An order of magnitude runtime improvement is provided over legacy methods with less than 10% error introduced. All QIST results are shown to be in-family with legacy methods. The tradespace for optimal delta-v design is found to range from 77.0 to 93.9 m/s, while the range of optimal dispersion is between 1.4 and 11.7 km.

INTRODUCTION

The goal of the present research is to demonstrate the utility of nonlinear relative motion modeling for the solution of operationally representative robust nonlinear optimization problems. Since at least the foundational work of Pitkin in 1966, higher order partials of the dynamical flow around an orbit have been recognized to have utility for a range of spaceflight problems.[1] Although mathematical techniques outside the traditional engineering curriculum can be required for keeping track of higher order partials of the dynamical flow, the theoretical, methodological groundwork for the use of state transition tensors (STTs) was further advanced after Park's doctoral work in 2007.[2] However, recent developments have focused on improving the feasibility of using second- and higher-order solutions in practice, as the curse of dimensionality plagues these techniques with slowed integration times and increased memory demands.[3–6] The distinctive feature of the Quadratic Interpolated State Transition (QIST) model is that a minimum necessary set of the STTs needed to compute arbitrary motion between any two times are computed once and interpolated. The resulting motion model is relative to a reference trajectory provided in a SPICE kernel, using a generalized

[*]Doctoral Candidate, Department of Aerospace Engineering and Engineering Mechanics, University of Texas at Austin, Austin, TX 78712. david.cunningham@utexas.edu

[†]Professor, Department of Aerospace Engineering and Engineering Mechanics, University of Texas at Austin, Austin, TX 78712. ryan.russell@austin.utexas.edu

[‡]Aerospace Engineer, GN&C Autonomous Flight Systems Branch, NASA Johnson Space Center, Houston, TX 77058. david.c.woffinden@nasa.gov

dynamics model incorporating a wide range of gravitational perturbations.[7] It is possible to use QIST for targeting in at least two modes: first, a target spacecraft's trajectory can be used as the reference kernel. A chaser spacecraft's trajectory is then computed, targeted, and/or optimized relative to the target. This first mode represents a relative motion problem and is the one used here. Additionally, a QIST model can be used to compute, target, and/or optimize updates to the trajectory stored within the kernel itself, treating the relative trajectories computed by QIST as alternatives to the reference. This mode is similar to a higher-order extension of the Generalized Reference Targeting paradigm.[8] Of course, the region of validity is limited in both modes to the region of quadratic convergence around the original reference trajectory.

Navigation errors, disturbance accelerations, burn execution biases and misalignments, and orbit insertion dispersions, are only a few examples of the host of uncertainty sources affecting a space mission. Incorparating this uncertainty into the design of a trajectory profile to make it robust to unknown perturbations is becoming more feasible, particularly with the maturation of linear covariance analysis (LinCov)[9,10] for closed-loop GN&C systems. LinCov is an analytic technique for predicting stochastic behavior of dynamical systems. Previous studies interfaced a genetic algorithm (GA) with a linear covariance analysis tool to provide the initial demonstration of applying this non-traditional approach to robust trajectory optimization. These robust trajectory design techniques were originally developed for rendezvous applications in low Earth orbit.[11] It was then extended to cislunar outbound trajectories to a Near Rectilinear Halo Orbit (NRHO)[12] and introduced for a simple rendezvous approach trajectory in the NRHO for mid-course correction placement.[13] Recently, these robust trajectory optimization principles have been applied to solve cislunar transfers to low-lunar orbit,[14] NRHO rendezvous and docking,[15] angles-only navigation for NRHO rendezvous,[16] lunar powered descent and landing,[17] along with Mars aerocapture[18] problems. They were also utilized to determine the optimized trajectory correction burn placement for the upcoming Artemis II free-return cis-lunar trajectory profile[19] and exercised to determine the optimized trajectory correction burn placement for NRHO orbit maintenance anticipated for the Artemis III mission.[20] Alternate robust trajectory optimization techniques that use a sweeping gradient method for ordinary differential equations with events (SGM) have been demonstrated.[21,22] SGM is a method for computing the gradient of trajectory analyses defined by performance indices over initial value problems with events with respect to static parameters.[23] A key to all these applications is having a fast yet reliable method to generated the integrated GN&C performance data. QIST is introduced here to provide this role for a wide spectrum of spaceflight missions.

The demonstrated problems in this paper include robust optimization scenarios that incorporate the trajectory dispersion due to both measurement and process noise through LinCov techniques. In particular, the return profile from the lunar surface to a Near Rectlinear Halo Orbit (NRHO) planned for future Artemis missions is modeled starting from one hour after the low lunar orbit departure (LLOD) burn to docking with a target vehicle representing the Gateway (GW), all in a relative motion context. First, the validity region of the QIST model in this scenario is examined. Second, a baseline trajectory including maneuver, covariance, and dispersion data is presented. Next, the optimization of trajectory correction maneuvers (TCMs) along this trajectory is performed with respect to two objective functions: Minimum maneuver magnitude only and minimum dispersion at a target point only. Finally, optimization with respect to objective functions consisting of convex combinations of maneuver magnitude and minimum dispersion are considered, and the sensitivity of the optimal trajectory to the objective function is examined. the primary contribution to the literature is the use of a kernel-referenced nonlinear relative motion model to perform robust trajectory

optimization in an operationally relevant context.

PROBLEM DESCRIPTION

After departing the surface of the Moon, Artemis astronauts in the human landing system (HLS) will return to a low lunar orbit (LLO). The Orion vehicle for returning to Earth will be in a near-rectilinear halo orbit (NRHO), specified by NASA.[24] The HLS will depart the LLO to rendezvous with the station, using one major LLOD maneuver and two optional mid-course TCMs to target an NRHO insertion point (NRI) located at the coordinates

$$\boldsymbol{r}_{NRI} = \begin{bmatrix} 0 & 100 & 100 \end{bmatrix}^T \text{ km} \tag{1}$$

in the Gateway Sun-referenced local vertical-local horizontal (S-LVLH) frame. The TCMs are nominally zero, so they are only carried out to correct trajectory errors introduced by LLOD or unmodeled dynamics/process noise, or to incorporate navigation information obtained during the pre-NRI phase. This operations concept is depicted in Fig. 1. The NRI point remains constant in

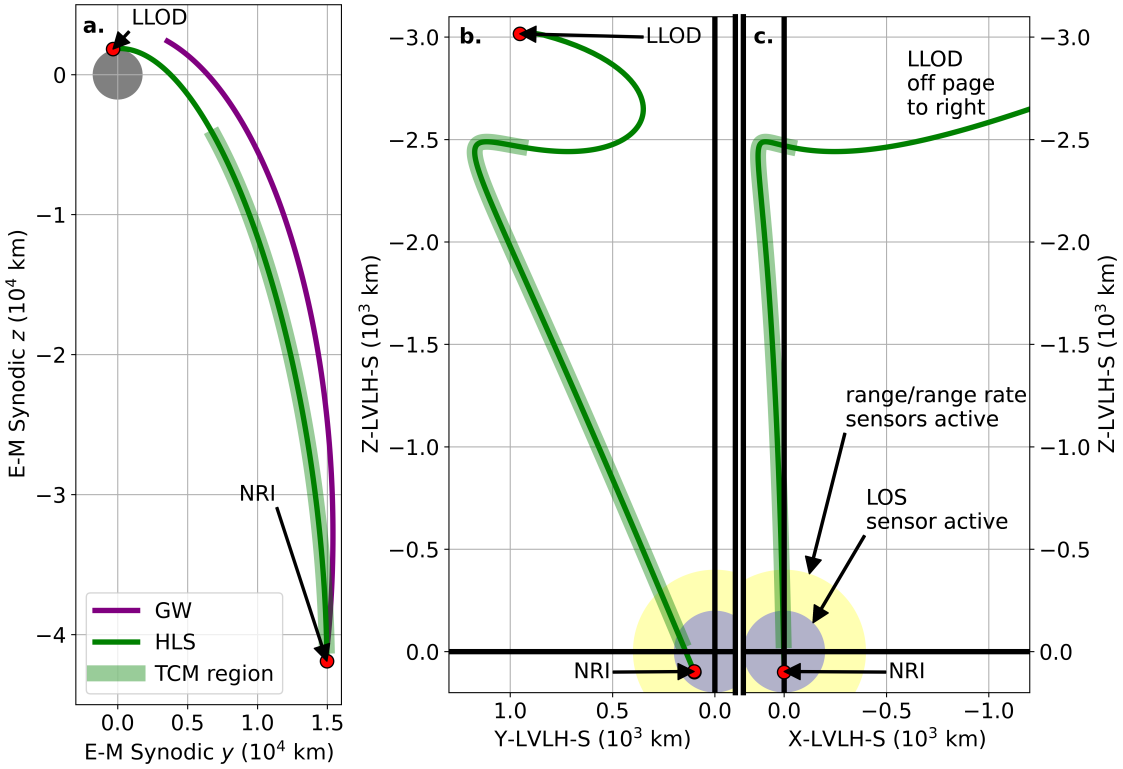

Figure 1. Nominal Lunar Departure Phase for Artemis with Optimization Domain in Shaded Green Bar. Left: Earth-Moon synodic frame. Center: GW centered S-LVLH, Y-Z plane. Right: GW centered S-LVLH, X-Z plane.

the S-LVLH frame regardless of the epoch of the scenario. Additionally, the time of arrival at NRI is fixed by mission constraints to LLOD + 24 hours. Subsequent to NRI, a series of rendezvous and proximity operations maneuvers will bring the HLS to docking with the Gateway. Since it occurs so far from perilune and at small relative distances and velocities, the post-NRI flight phase is well modeled by traditional linear relative motion methods. However, in the present study this part of the

flight phase is still modeled to demonstrate that QIST enables the consideration of the entire flight phase from shortly after LLOD in a single, unified dynamics framework.

Thus, the problem at hand is to design the two TCMs that will cause the HLS to arrive at NRI at a pre-specified epoch minimizing both delta-v and navigation dispersion errors. The timing, magnitude, and direction of the two TCMs are free variables. Recall that propagation of the QIST relative motion model across a ballistic segment is performed with a few vector-matrix-tensor operations in lieu of an ODE solution method.[25] Therefore, the QIST model of SPICE kernel relative motion provides the accuracy and speed necessary to carry out this optimization as part of the mission design process.

Measurement Model

The GN&C system uses a simplified measurement model intended to be representative of realistic conditions, yet not overly cumbersome for the current purpose. All of the measurements are relative between the HLS vehicle and Gateway. Four sensor types are modeled, with their properties summarized in Table 1. The ground navigation derived relative position and velocity measurements

Table 1. Relative Measurement Types During HLS Return RPOD

Sensor Type	Relative Measurement	Min Range	Max Range	Measurement Accuracy (σ)	Measurement Interval (Δt)
Ground Navigation	Position	400 km	N/A	1167 m per axis	30 min
	Velocity	400 km	N/A	0.25 m/s per axis	30 min
S-band Communication	Range	0.5 km	400 km	16.7 m	60 sec
	Range-rate	0.5 km	400	0.167 m/s	60 sec
Camera	LOS angles	0.1 km	200 km	0.025 deg per axis	60 sec
Lidar	Position	0.0 km	2 km	10.0 m per axis	30 sec

are grouped into a relative state measurement. This group emulates a lower accuracy relative measurement but they have a longer operational range to support the relative state estimation. The range and range-rate measurements that represent a radio-based navigation system are in a group with a reduced operational range but have increased accuracy. The LOS angle measurement modeling an onboard optical navigation camera, compliments the S-band communication range and range-rate data in this second group available at hundreds of kilometers. Lastly, the relative position measurement from a Lidar provides the greatest accuracy but the range of operation is within several kilometers. Fig. 1 b. shows the points at which the S-band communication and optical camera are engaged.

Dynamics Model

The HLS dynamics are modeled using QIST.[7] The force model captures the second order effects of Moon, Earth, Sun, and Jupiter gravity including an 8×8 spherical harmonics gravitational field. As previously reported, QIST generates quadratic relative motion models based on a reference trajectory relative to a SPICE kernel.[7] In this case, the reference trajectory is the NASA Gateway reference kernel.[24] Two equations used by the QIST model are relevant for the purposes of the robust optimization considered here. First, the relative state $\boldsymbol{\delta x}_a$ at a time t_a is propagated to a relative

state $\boldsymbol{\delta x}_b$ at a time t_b using a quadratic update

$$\boldsymbol{\delta x}_b = \boldsymbol{\Phi}_{ba}\boldsymbol{\delta x}_a + \frac{1}{2}\boldsymbol{\delta x}_a^T \underline{\boldsymbol{\Phi}}_{ba}\boldsymbol{\delta x}_a \tag{2}$$

where $\boldsymbol{\Phi}_{ba}$ and $\underline{\boldsymbol{\Phi}}_{ba}$ are the state transition matrix (STM) and second order state transition tensor (STT) of the Gateway dynamical flow between t_a and t_b. The STM and STT are obtained from precomputed interpolation coefficients from the reference orbit, along with transformations to map between two specific times. The tensor multiplication is a product over the last two indices of the STT. Eq. 2 is used to propagate the nominal trajectory. Second, the covariance matrix of the relative state $\boldsymbol{P}$ is propagated using

$$\boldsymbol{P}(t_b) = \boldsymbol{\Psi}_{ba}(\boldsymbol{\delta x_a})\boldsymbol{P}(t_a)\boldsymbol{\Psi}_{ba}^T(\boldsymbol{\delta x_a}) + \boldsymbol{Q} \tag{3}$$

where $\boldsymbol{Q}$ is a process noise matrix, constant in this model, and $\boldsymbol{\Psi}_{ba}(\boldsymbol{\delta x}_a)$ is the STM of the relative trajectory $\boldsymbol{\delta x}(t)$ computed using

$$\boldsymbol{\Psi}_{ba}(\boldsymbol{\delta x}_a) = \boldsymbol{\Phi}_{ba} + \underline{\boldsymbol{\Phi}}_{ba}\boldsymbol{\delta x}_a \tag{4}$$

The quantity $\boldsymbol{\Psi}_{ba}(\boldsymbol{\delta x}_a)$ is also used for linear maneuver targeting by LinCov. For greater depth on the topic of kernel relative motion and STT models, the cited references provide full details.[2,7,25]

The process noise model is Gaussian, zero mean, and with covariance given by:

$$\boldsymbol{Q} = q_r \begin{bmatrix} \left(\frac{\Delta t^3}{4}\right)\boldsymbol{I}_{3\times3} & \left(\frac{\Delta t^2}{2}\right)\boldsymbol{I}_{3\times3} \\ \left(\frac{\Delta t^2}{2}\right)\boldsymbol{I}_{3\times3} & (\Delta t)\,\boldsymbol{I}_{3\times3} \end{bmatrix} \tag{5}$$

where $q_r = 1.5 \times 10^{-7}$ m^2/s^3. Additionally, thruster firings are also subject to zero mean Gaussian noise with covariance matrix:

$$\boldsymbol{S} = s\boldsymbol{I}_{3\times3} \tag{6}$$

where $s = 0.044$ m/s. The parameters q_r and s were intended to be operationally representative of a crewed vehicle with realistic thrusters.

Performance Metrics

To perform robust trajectory optimization on trajectory correction maneuvers during a lunar lander return phase, several key performance metrics must be defined to objectively quantify acceptable performance. These metrics are derived from four states illustrated in Figure 2. The first is the true state $\mathbf{x}$ which is an n-dimensional vector that represents the *real world* environment or actual state. The nominal state $\bar{\mathbf{x}}$ is another n-dimensional vector that represents the desired or reference state. The navigation state $\hat{\mathbf{x}}$ is an $\hat{n}$-dimensional vector ($\hat{n} < n$) that represents the filter's estimated state. The design state x, often assumed to be the true state, is used to design the onboard navigation filter.

The variations between these states constitute the actual performance metrics considered in this analysis, also depicted in Figure 2. These include the true trajectory dispersions $\delta\mathbf{x}$, the navigation dispersions $\delta\hat{\mathbf{x}}$, the true navigation error $\delta\mathbf{e}$, and the onboard navigation error $\delta\hat{\mathbf{e}}$. The true dispersions $\delta\mathbf{x}$ are defined as the difference between the true state $\mathbf{x}$ and the nominal state $\bar{\mathbf{x}}$. The

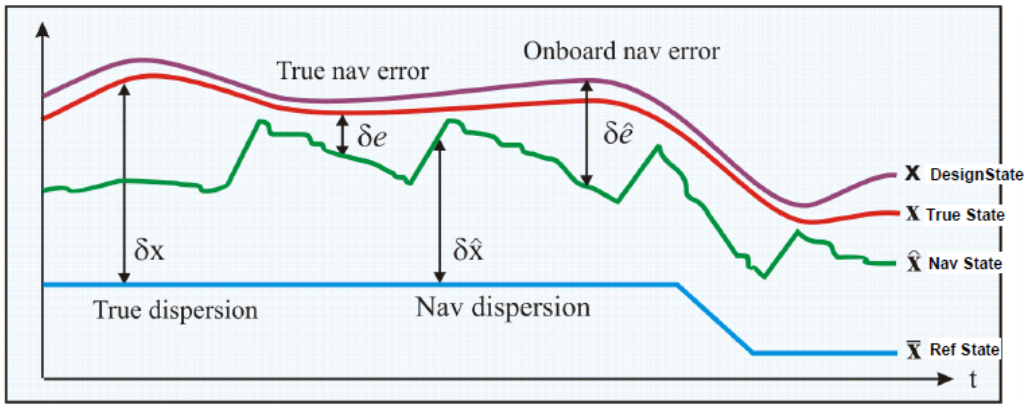

Figure 2. GN&C performance metric variables

covariance matrix of the true dispersions, $\mathbf{D}$, indicates how precisely a GN&C system can follow a desired trajectory.

$$\delta\mathbf{x} \triangleq \mathbf{x} - \bar{\mathbf{x}} \qquad \mathbf{D} = E\left[\delta\mathbf{x}\delta\mathbf{x}^{\mathrm{T}}\right] \tag{7}$$

The navigation dispersions $\delta\hat{\mathbf{x}}$ are defined as the difference between the navigation state $\hat{\mathbf{x}}$ and the nominal state $\bar{\mathbf{x}}$. The covariance of the navigation dispersions, $\hat{\mathbf{D}}$, reflects how precisely the onboard system thinks it can follow a prescribed reference trajectory.

$$\delta\hat{\mathbf{x}} \triangleq \hat{\mathbf{x}} - \mathbf{M}_x\bar{\mathbf{x}} \qquad \hat{\mathbf{D}} = E\left[\delta\hat{\mathbf{x}}\delta\hat{\mathbf{x}}^{\mathrm{T}}\right] \tag{8}$$

The matrix $\mathbf{M}_x$ is an $(\hat{n} \times n)$ matrix that maps the estimated state in terms of the true and nominal state. This matrix is necessary to account for the differences in vector length for $\hat{\mathbf{x}}$ and $\bar{\mathbf{x}}$.

The true navigation error $\delta\mathbf{e}$ is the difference between the true state and navigation state. It can also be calculated using the difference between the true dispersions and navigation dispersions. The covariance of the true navigation error, $\mathbf{P}$, quantifies how precisely the onboard navigation system can estimate the true state.

$$\delta\mathbf{e} \triangleq \mathbf{M}_x\mathbf{x} - \hat{\mathbf{x}} = \mathbf{M}_x\delta\mathbf{x} - \delta\hat{\mathbf{x}} \qquad \mathbf{P} = E\left[\delta\mathbf{e}\delta\mathbf{e}^{\mathrm{T}}\right] \tag{9}$$

The onboard navigation error $\delta\hat{\mathbf{e}}$ itself is never computed, but it is used to develop the onboard navigation filter equations. It is defined as the difference between the design state, x, and the navigation state $\hat{\mathbf{x}}$. The covariance of the onboard navigation error, $\hat{\mathbf{P}}$, quantifies how precisely the onboard navigation system expects it can determine the actual state. The performance of the onboard navigation system is determined by comparing $\hat{\mathbf{P}}$ to the actual navigation performance $\mathbf{P}$.

$$\delta\hat{\mathbf{e}} \triangleq \mathrm{x} - \hat{\mathbf{x}} \qquad \hat{\mathbf{P}} = E\left[\delta\hat{\mathbf{e}}\delta\hat{\mathbf{e}}^{\mathrm{T}}\right] \tag{10}$$

If the *true* states and the *design* states are assumed to be the same (such as in this paper), then the true navigation covariance will equal the onboard navigation covariance.

The covariance matrices of the true dispersions, navigation dispersions, true navigation error, and the onboard navigation error are ultimately used to analyze and assess the performance of a proposed

GN&C system. A common approach to obtain these performance metrics is to use a Monte Carlo simulation outlined in Figure 3, where the sample statistics of hundreds or thousands of runs, N, are used to numerically compute the desired covariance matrices.

$$\mathbf{D} = \frac{1}{N-1}\sum \delta\mathbf{x}\delta\mathbf{x}^{\mathrm{T}} \qquad \hat{\mathbf{D}} = \frac{1}{N-1}\sum \delta\hat{\mathbf{x}}\delta\hat{\mathbf{x}}^{\mathrm{T}} \qquad \mathbf{P} = \frac{1}{N-1}\sum \delta\mathbf{e}\delta\mathbf{e}^{\mathrm{T}} \tag{11}$$

The onboard navigation error covariance $\hat{\mathbf{P}}$ is the navigation filter covariance for each run. This

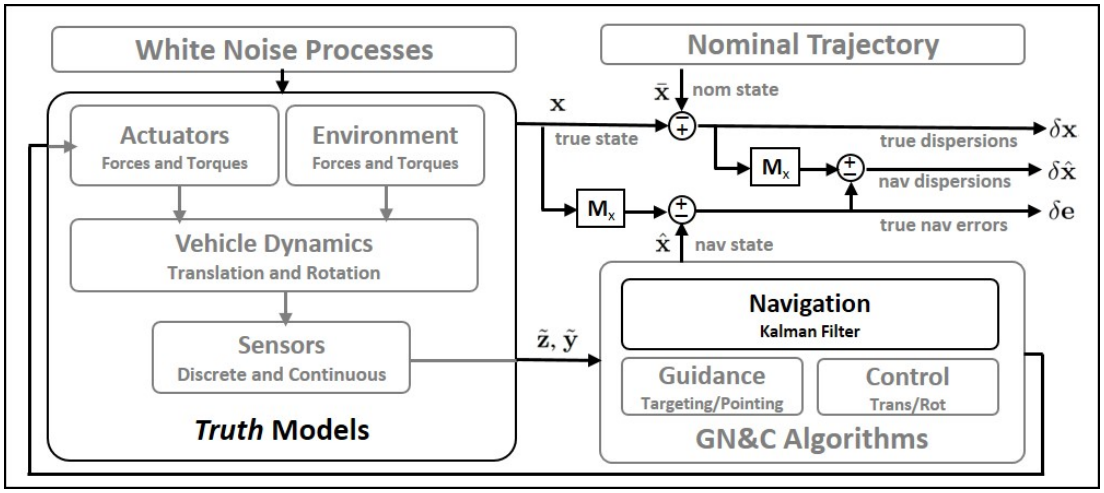

Figure 3. Extracting GN&C performance metrics using Monte Carlo techniques

same statistical information can be obtained using linear covariance analysis techniques. Linear covariance analysis incorporates the non-linear system dynamics models and GN&C algorithms to generate a nominal reference trajectory $\bar{\mathbf{x}}$ which is then used to propagate, update, and correct an onboard navigation covariance matrix $\hat{\mathbf{P}}$ and an augmented state covariance matrix $\mathbf{C}$,

$$\mathbf{C} = E\left[\delta\mathbf{X}\delta\mathbf{X}^{\mathrm{T}}\right] \tag{12}$$

where the augmented state $\delta\mathbf{X}^{\mathrm{T}} = [\delta\mathbf{x}^{\mathrm{T}}\ \delta\hat{\mathbf{x}}^{\mathrm{T}}]$ consists of the true dispersions and the navigation dispersions. Pre- and post-multiplying the augmented state covariance matrix by the following mapping matrices, the covariance matrices of the trajectory dispersions, navigation dispersions, and the navigation error can be obtained with a single simulation run.

$$\begin{aligned}
\mathbf{D} &= [\,\mathbf{I}_{n\times n},\ \mathbf{0}_{n\times\hat{n}}\,]\,\mathbf{C}\,[\,\mathbf{I}_{n\times n},\ \mathbf{0}_{n\times\hat{n}}\,]^{\mathrm{T}} \\
\hat{\mathbf{D}} &= [\,\mathbf{0}_{\hat{n}\times n},\ \mathbf{I}_{\hat{n}\times\hat{n}}\,]\,\mathbf{C}\,[\,\mathbf{0}_{\hat{n}\times n},\ \mathbf{I}_{\hat{n}\times\hat{n}}\,]^{\mathrm{T}} \\
\mathbf{P} &= [\,\mathbf{I}_{\hat{n}\times n},\ -\mathbf{I}_{\hat{n}\times\hat{n}}\,]\,\mathbf{C}\,[\,\mathbf{I}_{\hat{n}\times n},\ -\mathbf{I}_{\hat{n}\times\hat{n}}\,]^{\mathrm{T}}
\end{aligned} \tag{13}$$

Eq. 2 and Eq. 3, along with LinCov analysis equations not summarized here, are used to propagate, update, and correct the augmented state covariance matrix and the onboard navigation covariance matrix. For a deeper analysis of the construction, development, and application of the LinCov simulation, see the cited references.[9,10,26–29]

Optimization Problem and Method

Consistent with previous research, a genetic algorithm (GA) is used in order to conduct the nonlinear optimization of the maneuvers. A GA is a type of optimization solver which employs evolutionary processes to search a solution space.[30] A population of candidates is generated, evaluated, and based on their performance a new generation is created by combining and mutating them. During each iteration, candidate values of the optimization variables are passed to the LinCov simulation, which is then evaluated to determine the values of the cost and penalty functions. The TCM burns are error-correction burns, so the expected value of their magnitudes is defined to be zero, i.e. no TCMs are required along the nominal trajectory. Thus, the optimization variables for this problem are t_1 and t_2, the ignition time (tig) of the first and second TCMs. The objective functions for optimization are a family of functions $J_w : \mathbb{R}^2 \times [0,1] \to [0,\infty)$:

$$J_w(t_1,t_2) = J(t_1,t_2;w) = w n_v \Delta v_{3\sigma}(t_1,t_2) + (1-w) n_d \left|\boldsymbol{\delta r}_{NRI}(t_1,t_2)\right| \tag{14}$$

where $\Delta v_{3\sigma}$ is the accumulated 3 standard deviation bound of delta-v across all maneuvers, accounting for process and measurement noise in the LinCov model, $\boldsymbol{\delta r}_{NRI} = \begin{bmatrix}\sigma_{xx} & \sigma_{yy} & \sigma_{zz}\end{bmatrix}^T$ is the position dispersion vector at NRI, n_v and n_d are velocity and dispersion normalizing parameters, and w is a weighting parameter to indicate preference to give to either the burn magnitude or position dispersion at NRI. In general, the optimization problem for a given value of w is:

$$\begin{aligned} \underset{t_1,\,t_2}{\text{minimize}} \quad & J_w(t_1,t_2) \\ \text{subject to} \quad & t_2 - t_1 \geq 1 \text{ hr} \\ & t_1 - t_0 \geq 0 \\ & t_f - t_2 \geq 1 \text{ hr}. \end{aligned}$$

In the case where $w = 0$ and only position dispersions are considered, the optimal time of the TCMs is expected to move as close to NRI as possible to take maximum advantage of the more accurate navigation information. On the other hand, when $w = 1$ and only the $\Delta v_{3\sigma}$ is considered, the optimal TCMs location is expected to move as close to LLOD as possible in order to achieve the greatest change to the final state for a given amount of delta-v.

The GA process is summarized in Figure 4. For each of the optimization runs performed using

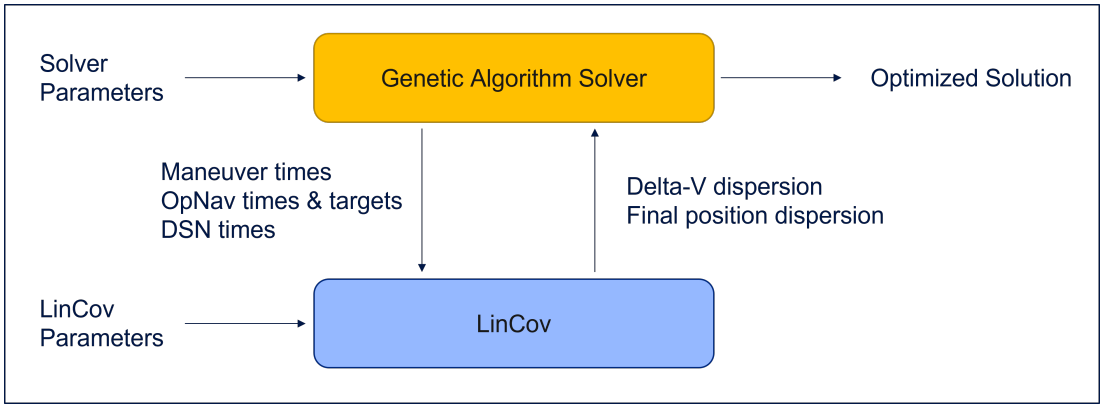

Figure 4. Functional relationship between the LinCov simulation and Genetic Algorithm.

the genetic algorithm, a population size of 500 was selected along with a maximum generation of 200.

RESULTS

First, the QIST model is validated for the Artemis Lunar ascent rendezvous scenario. Next, the edge cases for the optimization are shown, namely the delta-v optimal and NRI-dispersion optimal trajectories are detailed. Finally, the weighting parameter w is varied from 0 to 1 and the behavior of the optimal TCM locations is discussed.

Validity Region of QIST model

Since the optimization is performed entirely within the context of QIST dynamics, it is useful to understand how accurately the QIST model replicates an HLS baseline trajectory numerically integrated in an inertial ephemeris model. The force model used for both numerical integration and QIST propagation of HLS trajectories is as close as possible to the model used for the Gateway reference kernel, i. e. it includes the Keplerian gravitational influence of the Moon, Earth, Sun, and Jupiter Barycenter along with an 8×8 spherical harmonics gravity model based on GRAIL data.[24]

From the baseline HLS state at the NRI point, the QIST trajectory is propagated backwards in time using both a linear and a quadratic propagation step. Disagreement between the baseline and QIST propagated position and velocity are normalized by their baseline values and plotted as a function of time in Fig. 5. The results are considered to have diverged from each other when they disagree by more than 10% in either relative position or relative velocity.

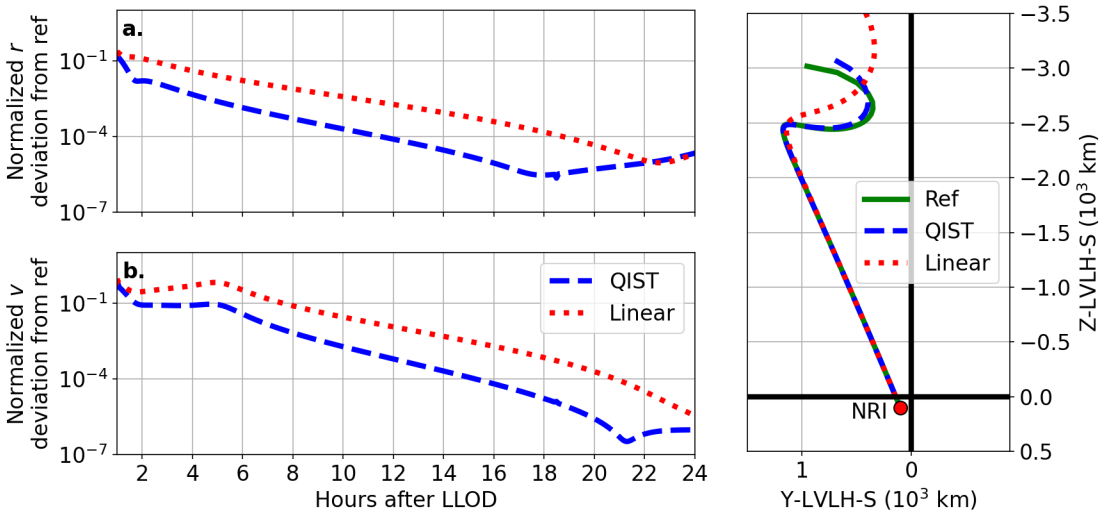

Figure 5. Performance of free-drift QIST and Linear Relative Motion Models vs. Baseline. a: Deviation of QIST and linear relative position from baseline. b: Deviation of QIST and linear relative velocity from baseline. c: S-LVLH View of Baseline, QIST, and Linear NRI Approach Trajectories.

As Fig. 5 shows, the QIST model remains in-family with the baseline model for all times after LLOD + 1 hour. Note that exquisite accuracy of the QIST model is not needed or expected in order

to produce valid optimization results–The goal is to obtain the qualitative behavior of the TCM timing in a quadratic relative motion model that can provide information to mission planners. In consideration of these validity results, and taking into account that time is likely needed for orbit determination after a large LLOD maneuver, the optimization scenarios considered in this work start at LLOD + 3 hours.

Scenario Baseline

The end-to-end nominal rendezvous trajectory in the relative Sun-referenced LVLH (S-LVLH) frame starting two hours following LLOD to docking contact using QIST is illustrated in Fig. 6. The far-field rendezvous profiles in both the YZ-plane and XZ-plane are captured in Fig. 6(a) and Fig. 6(b) respectively with the arbitrary baseline correction burn locations for C1 (3 hours following LLOD) and C2 (5 hours prior to NRI) indicated with solid red dots. The arrival time at NRI is LLOD + 24 hours at a relative distance of 141 km from the Gateway. Following the NRI burn, the plane of motion is the YZ-plane and the subsequent relative profile is fixed regardless of the lunar ascent epoch. Details related to the in-plane rendezvous profile following NRI to dock are captured in Fig. 6(c) and Fig. 6(d). The docking axis of Gateway is acquired at 1 km which initiates the final approach and docking sequence. The nominal delta-v to complete the rendezvous sequence is 64.3 m/s with a total duration of 29.5 hours.

An overview of the integrated GN&C performance for the NRHO rendezvous is provided in Fig. 7 with a snap shot of the total delta-v captured in the top-left portion of the figure, the sensor measurement scheduling illustrated in the middle-left plot with dashed vertical lines indicating the various burn epochs, position and velocity navigation errors summarized in the bottom-left plots, position and velocity magnitude dispersions shown on the bottom-right images, and the in-plane trajectory profile with the 3-sigma performance ellipses in the top-right.

The unoptimized placement of the correction burns produces a total delta-v (nominal + 3-sigma) of 78.3 m/s with 3-sigma NRI position magnitude dispersions of 9.6 km. The arbitrary placement of the baseline correction burns placed C2 prior to any relative range, range-rate, or angle measurements being available. The timing of when burns are performed with regards to the navigation system ability to process accurate relative measurements plays an important role in identifying *optimized* burn epochs.

Optimization Results

Depending on the objective criteria, the *optimized* solution can have a large contrast of correction burn times as illustrated in Fig 8. For example, in Fig 8(a) the optimization is first carried out setting the weighting factor to zero, $w = 0$, optimizing only for the total delta-v. Consequently C2 is performed earlier to reduce the total delta-v by about 1 m/s to 77.0 m/s from the baseline of 78.3 m/s at the expense of larger NRI dispersions that increased by 2 km from 9.6 km to 11.7 km. Interestingly, the first correction burn, C1, is performed almost 2 hours later than the baseline time.

The other extreme is examined in Fig 8(b) where the weighting factor is set to one, $w = 1$, optimizing performance only for the position magnitude dispersion at NRI. To reduce the NRI dispersions, the C2 burn is delayed to the latest possible time interval where both the relative S-band and optical camera measurements become available to execute it more precisely. The impacts due to disturbance accelerations on the vehicle are also limited with a shorter transfer time between the last correction burn and NRHO insertion. The NRI dispersions are reduced by an order of

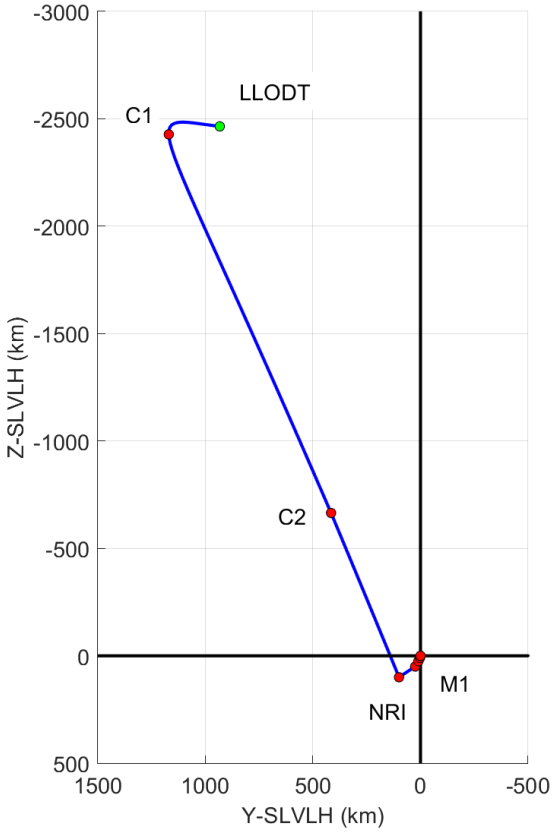

(a) LLOD YZ Profile

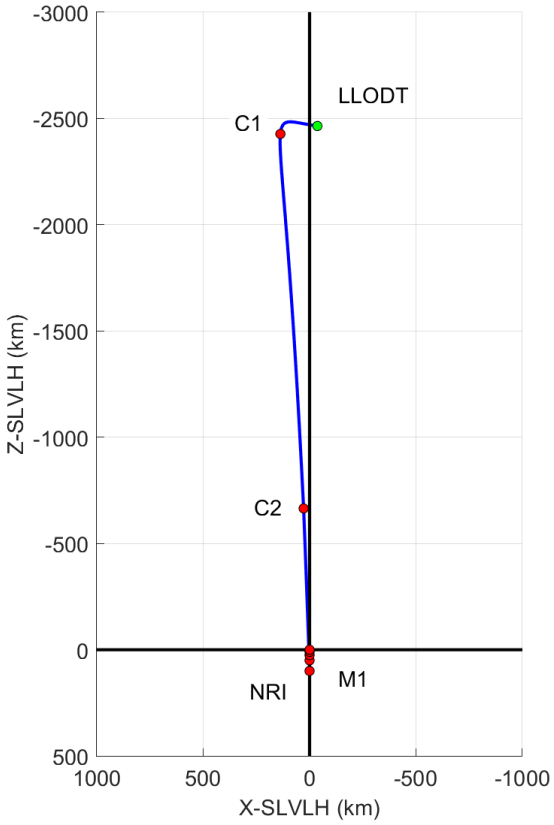

(b) LLOD XZ Profile

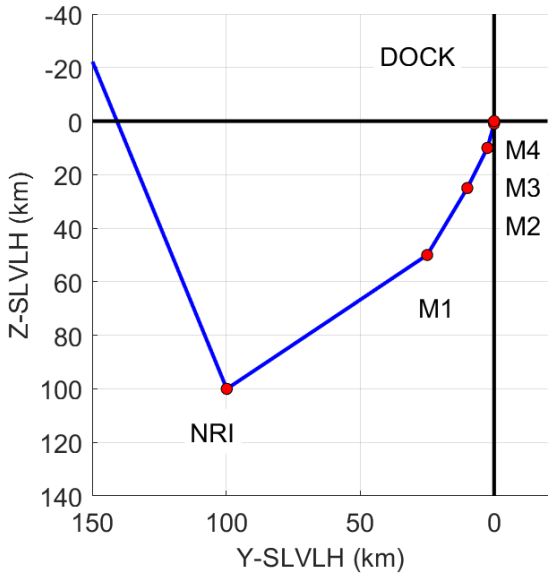

(c) NRI YZ Profile

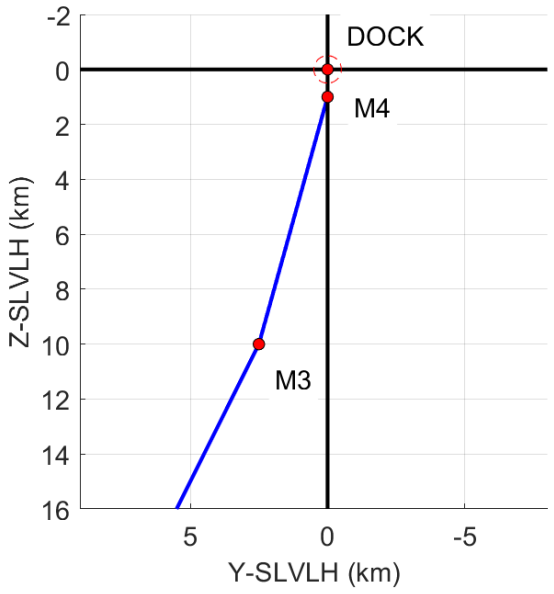

(d) M3 YZ Profile

Figure 6. NRHO Nominal Rendezvous Trajectory Scenario

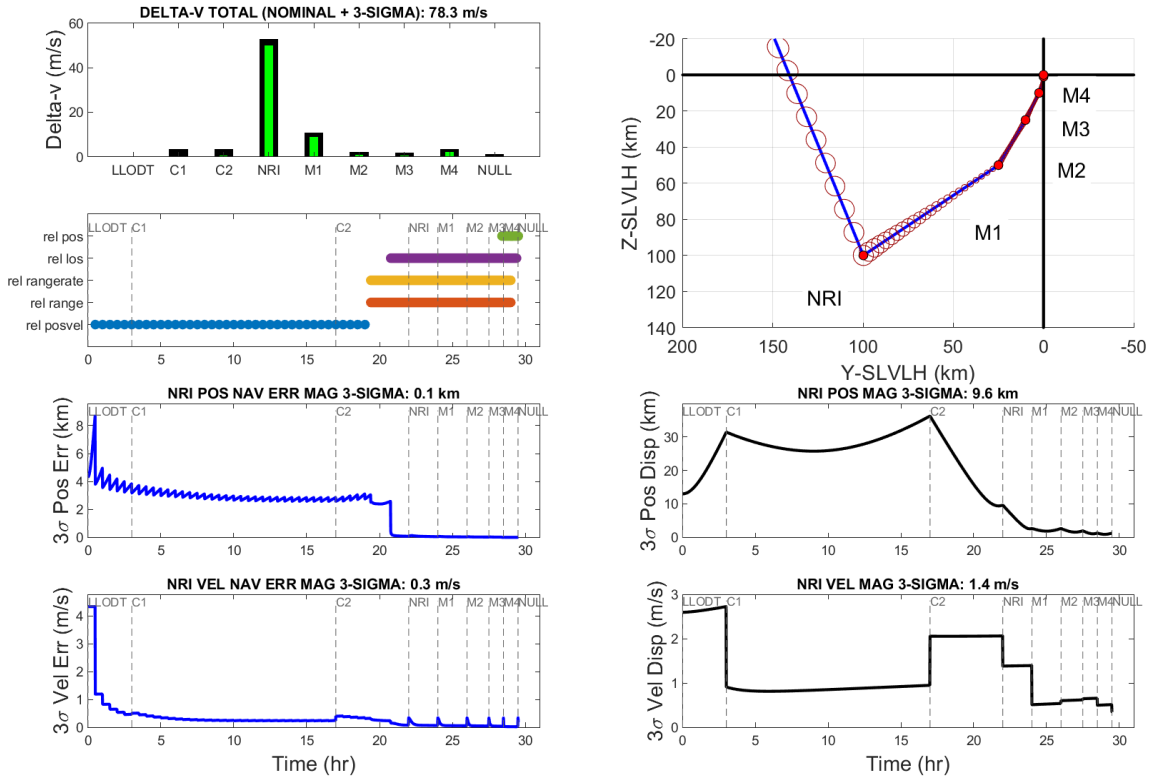

Figure 7. LinCov Summary Plot for Scenario Baseline

magnitude from about 10 km to a little over 1 km. Although the delay helps the NRI performance, it comes at a significant delta-v cost of almost 15 m/s. The delta-v impacts are largely experienced with the C2 and NRI burns.

This simple exercise highlights the needed balance between improving accuracies at NRI to support rendezvous and crew safety, while minimizing that necessary propellant to complete the mission. What is the proper balance? Or what is the appropriate weighting factor of priorities between these two opposing ideals? A natural and intuitive insight to the optimization problem emerges when investigating the sensitivity of the performance metrics as a function of different correction burn times, referred to as mission maps and illustrated in Fig 9.

The results of 10,000 different combinations of C1 and C2 times are depicted in Fig 9(a) as indicated with small blue dots. Since C1 occurs prior to C2, the trade space of options is limited to the top left triangle portion of the plot. The baseline burn times on the mission map are indicated with the solid red dot. The optimized burn placements with different weighting factors are marked with varying gray scale colors from white (w = 0, minimize total delta-v) to black (w = 1, minimize NRI position dispersions) circles.

Fig 9(b) gives context to the resulting correction burn placement with regards to the trajectory itself and the other baseline burn locations (marked with solid red dots). In general, the trend is to delay the correction burns, particularly C1, to both minimize delta-v and NRHO insertion dispersions relative to the notional baseline specifications.

The mission map highlighting the sensitivity of burn placement to total delta-v is provided in Fig

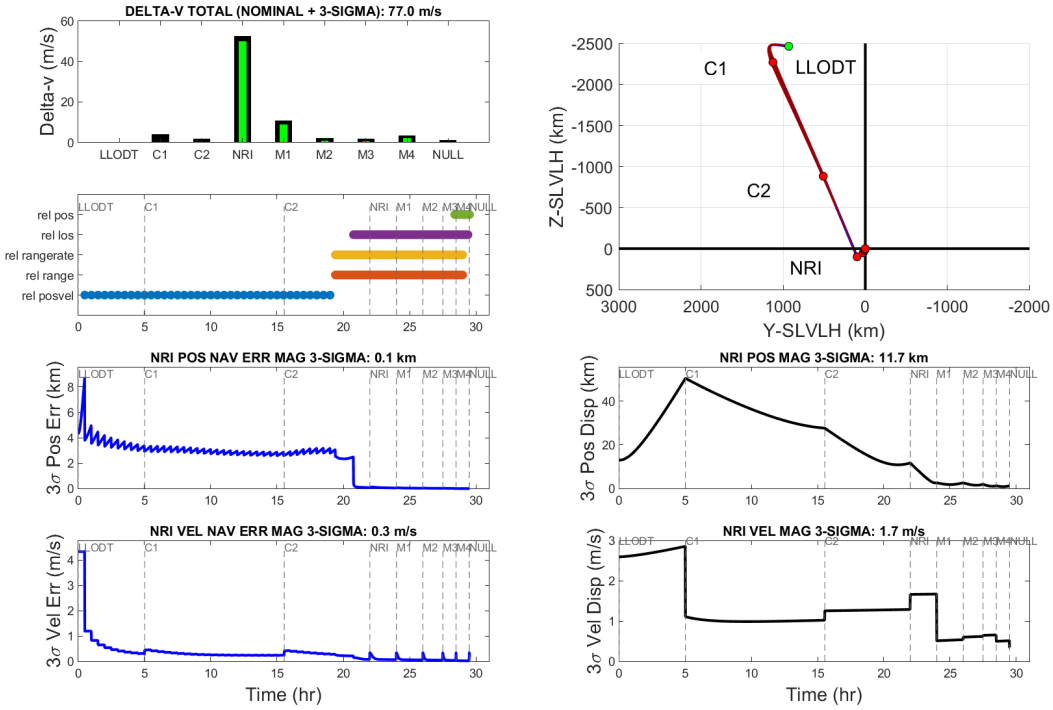

(a) Optimized Correction Burn Placement Results for Minimum 3σ Δv Magnitude

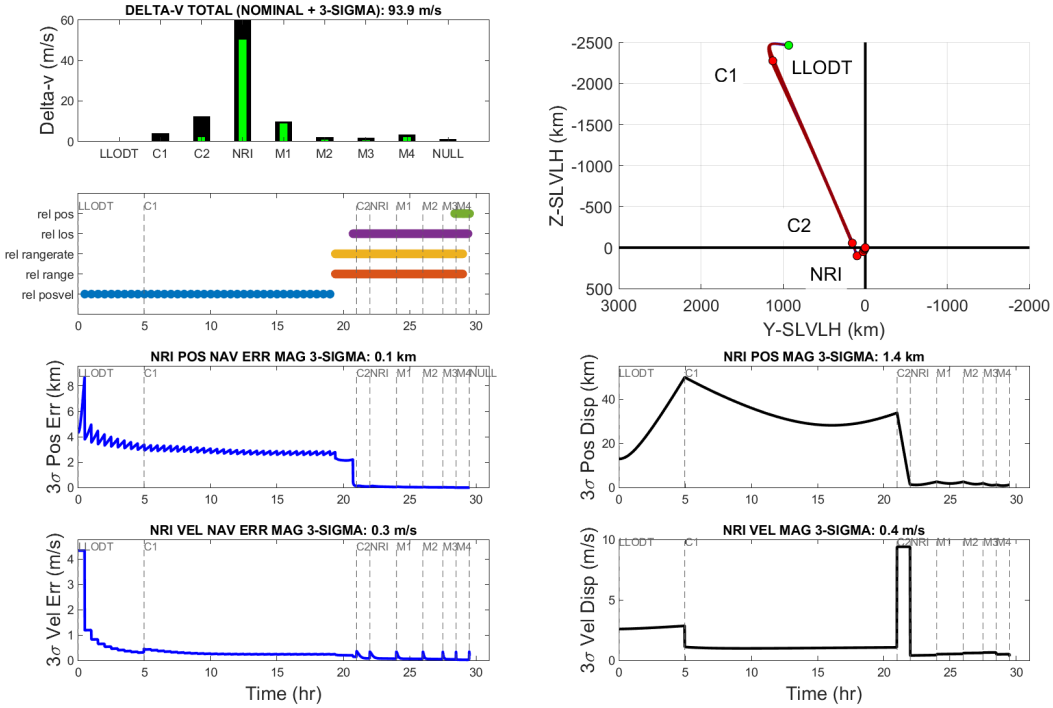

(b) Optimized Correction Burn Placement Results for Minimizing NRI position dispersion

Figure 8. Optimization Results for NRHO Transfer Correction Burn Placement

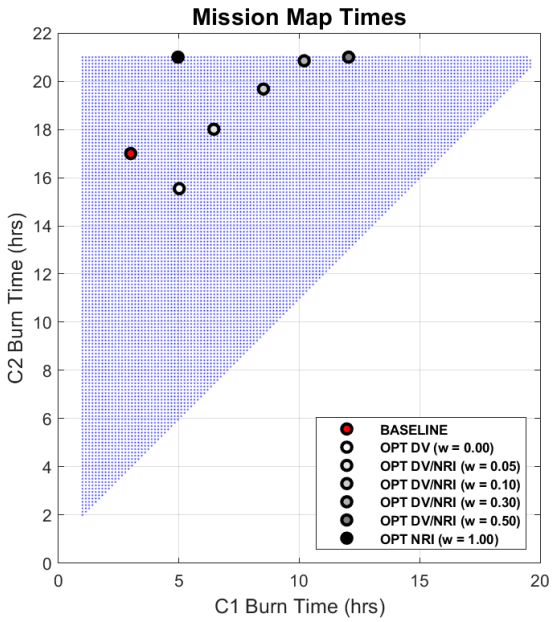

(a) Mission Map Trade Space

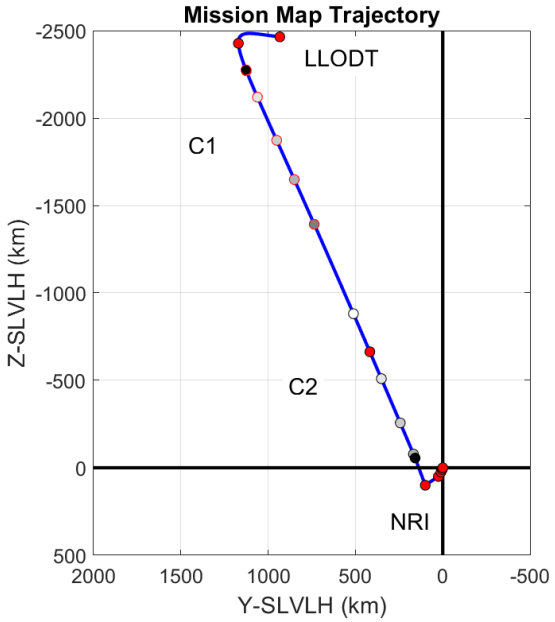

(b) Mission Map Trajectory Profile

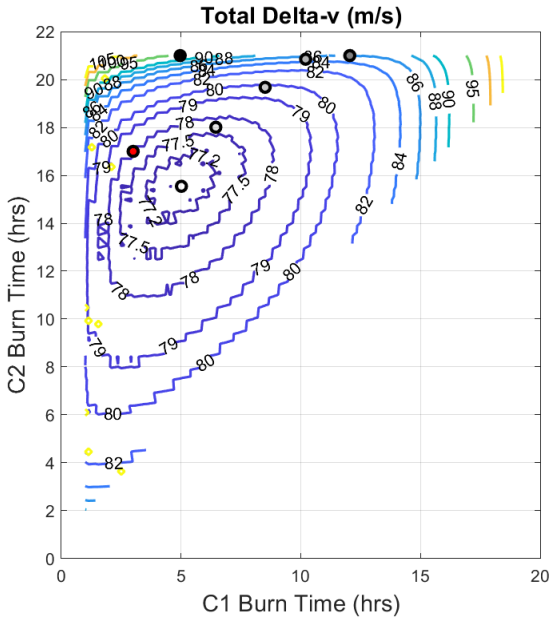

(c) Mission Map for Total Delta-v

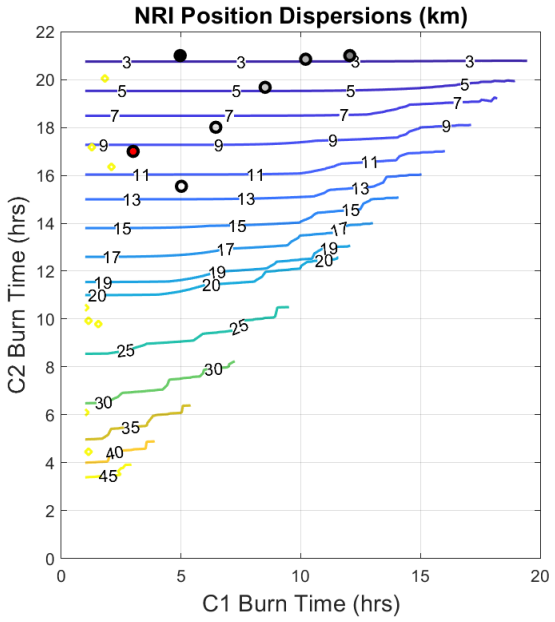

(d) Mission Map for NRI Position Dispersions

Figure 9. NRHO Rendezvous Mission Map

9(c). The contours and the numerical markings indicate bands of total delta-v (m/s) given different burn times. The baseline and *optimized* burns with different weights are also included with large solid filled dots. The optimization trends observed previously begin to have greater meaning given the delta-v mission map. With a weighting factor of zero when total delta-v is minimized (solid white circle), the placement is at the center of the minimum contour lines as expected.

A more complete understanding emerges as the mission maps for the NRI position dispersions in Fig 9(d) are also considered. As the weighting factor increases, it forces the objective function to also strive to minimize the position dispersions, not just total delta-v. As a consequence the burn time for C2 is delayed more and more along the NRI dispersion contour lines as the weighting factor increases. Even though the NRI dispersions are rather insensitive to the first correction burn placement, they are directly dependent on the timing of the second correction burn.

Given both mission maps in Fig 9(c) and Fig 9(d) the optimized placement of the correction burns becomes rather intuitive, even without a formal optimization algorithm. The mission maps highlight the sensitivities such that a mission designer or trajectory operations can instinctively identify the *best* burn placement given a myriad of mission priorities and factors that must be accounted for based on priorities. As the priority shifts from minimizing total delta-v (w = 0) the time of both C1 and C2 are delayed such that NRHO position dispersions are reduced while following the delta-v contours that require the least delta-v.

The extraction of these mission maps and the enabling technology that facilitates these robust trajectory optimization techniques is having a fast yet reliable method to produce the integrated GN&C performance metrics, such as total delta-v (nominal + 3-sigma) and trajectory dispersions. Several factors influence the speed of the process, but one aspect is having the means to capture the impact of the state dynamics, both on the nominal trajectory propagation, covariance propagation, and targeting. QIST provides a viable solution to providing an extremely fast solution and this research has begun to explore its potential and limitations.

The problem formulated for this study was selected for its simplicity. It allows these concepts to be demonstrated while allowing the complexity of the problem formulation to cloud the intuitive nature that can come to more sophisticated problems. These techniques can easily be scaled, but that scaling will require more time and resources, or techniques like QIST that can generate the performance metrics faster yet reliably.

CONCLUSION

The first application of motion relative to a SPICE kernel is presented. Starting with relative separation distances greater than the Lunar radius and relative speeds on the order of hundreds of meters per second and continuing to final docking approach, QIST enables almost the entire lunar ascent rendezvous phase to be considered as a unified whole. The accuracy needed for such an approach is provided by the second-order ephemeris dynamics of the QIST model. In addition, the fast computation speed of the relative trajectories is enabled by the use of STT dynamics in QIST rather than the traditional on-line numerical integration of the relative trajectories. When combined with LinCov techniques, these simulations found the optimal locations for two TCMs under a class of objective functions consisting of a convex combination of the position dispersion at NRI and the total 3σ delta-v needed, taking into account an operationally representative sensor model.

The QIST model results are found to be in-family with the ground-truth model, while providing an order of magnitude timing improvement over legacy methods. Over the period used in optimization, QIST introduces no more than 10% error, with most of the time period examined showing negligible difference between the ground-truth model and QIST. In all cases examined, QIST-propagated trajectories outperformed a linear equivalent.

These performance metrics are found to be in competition with each other, showing that minimizing delta-v led to an increase in dispersion and vice versa. The range of delta-vs for optimal

trajectories was between 77.0 and 93.9 m/s. The range of dispersions for optimal trajectories was between 1.4 and 11.7 km. In addition, the optimal delta-v and optimal dispersion solutions represent a 1.6% and 85% improvement, respectively, over the baseline case.

The QIST framework is demonstrated to enable acceptable dispersions for GW rendezvous. This paper presents the first application of kernel relative motion to an operational problem, but the applications of QIST and models like it are broader. The capability to contribute in a robust context is especially relevant for missions wit human crew where safety is paramount. A pure relative motion problem such as the one presented here is the driving design case for QIST, but applications to targeting problems, analysis, and optimization of the SPICE kernel trajectory itself are abundant, such as covariance analysis and rapid on board guidance in ephemeris dynamics models.

ACKNOWLEDGMENT

This work was supported in part by NASA Science and Technology Graduate Research Opportunity 80NSSC20K1213.

REFERENCES

[1] E. T. Pitkin, "Second Transition Partial Derivatives Via Universal Variables," *Journal of the Astronautical Sciences*, Vol. 13, Jan. 1966, p. 204.

[2] S. H. Park, *Nonlinear Trajectory Navigation*. PhD Thesis, University of Michigan, Ann Arbor, 2007.

[3] S. Boone and J. McMahon, "Directional State Transition Tensors for Capturing Dominant Nonlinear Effects in Orbital Dynamics," *Journal of Guidance, Control, and Dynamics*, Nov. 2022, pp. 1–12, doi:10.2514/1.G006910.

[4] J. Kulik, W. Clark, and D. Savransky, "FAST APPROXIMATION OF CONTINUOUS THRUST OPTIMAL RELATIVE CONTROL IN THE THREE BODY PROBLEM," Austin, TX, USA, Jan. 2022. Paper AAS 22-691.

[5] J. Kulik, W. Clark, and D. Savransky, "State Transition Tensors for Continuous-Thrust Control of Three-Body Relative Motion," *Journal of Guidance, Control, and Dynamics*, May 2023, pp. 1–10, doi:10.2514/1.G007311.

[6] J. Kulik and K. A. LeGrand, "Nonlinearity and Uncertainty Informed Moment-Matching Gaussian Mixture Splitting," Nov. 2024. arXiv:2412.00343 [stat], doi:10.48550/arXiv.2412.00343.

[7] D. Cunningham and R. P. Russell, "Relative Motion Solutions Around an Arbitrary SPICE Kernel Trajectory," *AAS/AIAA Astrodynamics Specialist Conference*, Denver, CO, USA, Aug. 2024. Paper AAS 24-457.

[8] D. Geller, D. Woffinden, and C. York, "Generalized Reference Targeting for Spaceflight," *AAS/AIAA Astrodynamics Specialist Conference*, North Logan, UT, AAS 25-099, 31 January - 3 February 2025.

[9] P. S. Maybeck, *Stochastic models, estimation, and control*, Vol. 1. New York: Academic Press, 1979.

[10] D. K. Geller, "Linear Covariance Techniques for Orbital Rendezvous Analysis and Autonomous Onboard Mission Planning," *Journal of Guidance, Control, and Dynamics*, Vol. 29, November-December 2006, pp. 1404–1414.

[11] K. Jin, D. K. Geller, and J. Luo, "Robust Trajectory Design for Rendezvous and Proximity Operations with Uncertainties," *Journal of Guidance, Control, and Dynamics*, Vol. 43, No. 4, 2020, pp. 741–753.

[12] D. K. Geller, S. Shuster, D. Woffinden, and S. Bieniawski, "Robust Cislunar Trajectory Optimization via Midcourse Correction and Optical Navigation Scheduling," *44th Annual AAS Guidance, Navigaiton and Control Conference*, Breckenridge, CO, AAS 22-065, 4-9 February 2022 2022.

[13] D. Woffinden, S. Shuster, and S. Geller, David Kand Bieniawski, "Robust Trajectory Optimization and GN&C Performance Analysis For NRHO Rendezvous," *2022 AAS/AIAA Astrodynamics Specialist Conference*, Charlotte, North Carolina, 22-564, 7-11 August 2022 2022.

[14] D. Geller, D. Woffinden, and S. Bieniawski, "Sensitivity of Optimal Midcourse Correction Scheduling for Robust Cislunar Trajectory Design," Breckenridge, CO, AAS 23-061, 1 Feb - 6 Feb 2023.

[15] T. Goulet, D. Woffinden, N. Collins, and B. Andrews, "Robust Trajectory Design for Rendezvous in a Near Rectilinear Halo Orbit," Breckenridge, CO, AAS 23-066, 1 Feb - 6 Feb 2023.

[16] T. Cavesmith, D. Woffinden, and N. Collins, "Angles-Only Robust Trajectory Optimization for NRHO Rendezvous," Breckenridge, CO, AAS 24-168, 2 Feb - 7 Feb 2024.

[17] G. Calkins, D. Woffinden, and Z. Putnam, "Robust Trajectory Optimization for Guided Powered Descent and Landing," *2022 AAS/AIAA Astrodynamics Specialist Conference*, Charlotte, NC, AAS 22-660, 7-11 August 2022 2022.

[18] J. Joshi, D. Woffinden, and Z. Putnam, "End-to-End Mars Aerocapture Analysis Using Linear Covariance Techniques and Robust Trajectory Optimization," *2022 AAS/AIAA Astrodynamics Specialist Conference*, Charlotte, NC, AAS 22-678, 7-11 August 2022 2022.

[19] D. Woffinden, R. Eckman, and S. Robinson, "Optimized Trajectory Correction Burn Placement for the NASA Artemis II Mission," Breckenridge, CO, AAS 23-062, 1 Feb - 6 Feb 2023.

[20] D. Woffinden and B. Barton, "Optimized Trajectory Correction Burn Placement for NRHO Orbit Maintenance," *33rd AAS/AIAA Space Flight Mechanics Meeting*, Austin, TX, AAS 23-364, 15 - 19 January 2023.

[21] B. W. L. Margolis and D. Woffinden, "Robust Trajectory Optimization Techniques Using a Sweeping Gradient Method and Linear Covariance Analysis," *AAS/AIAA Astrodynamics Specialist Conference*, Broomfield, CO, AAS 24-364, 11 - 15 August 2024.

[22] B. W. L. Margolis and D. Woffinden, "Co-Optimization of Navigation System Requirements and Trajectory Design Using a Sweeping Gradient Method and Linear Covariance Analysis," *AAS/AIAA Astrodynamics Specialist Conference*, Broomfield, CO, AAS 24-365, 11 - 15 August 2024.

[23] B. W. L. Margolis, "A Sweeping Gradient Method for Ordinary Differential Equations with Events," *Journal of Optimization Theory and Applications*, Vol. 199, Oct. 2023, pp. 600–638, 10.1007/s10957-023-02303-3.

[24] D. E. Lee, "National Aeronautics and Space Administration (NASA) White Paper: Gateway Destination Orbit Model: A Continuous 15 Year NRHO Reference Trajectory," tech. rep., NASA, 2019.

[25] D. Cunningham and R. P. Russell, "An Interpolated Second-Order Relative Motion Model for Gateway," *The Journal of the Astronautical Sciences*, Vol. 70, Aug. 2023, p. 26, doi:10.1007/s40295-023-00393-9.

[26] J. W. Williams, W. E. Brandenburg, D. C. Woffinden, and Z. R. Putnam, "Validation of Linear Covariance Techniques for Mars Entry, Descent, and Landing Guidance and Navigation Performance Analysis," *AIAA Scitech 2022 Forum*, 2022, doi:10.2514/6.2020-0597.

[27] D. Woffinden, S. Robinson, J. Williams, and Z. Putnam, "Linear Covariance Analysis Techniques to Generate Navigation and Sensor Requirements for the Safe and Precise Landing - Integrated Capabilities Evolution (SPLICE) Project," *AIAA Scitech 2019 Forum*, San Diego, CA, AIAA 2019-0662, 7-11 January 2019.

[28] T. J. Moesser and D. K. Geller, "Guidance and Navigation Linear Covariance Analysis for Lunar Powered Descent," *AAS/AIAA Astrodynamics Specialist Conference*, Mackinac Island, Michigan, AAS 07-313, 19-23 August 2007.

[29] D. Geller and D. Christensen, "Linear Covariance Analysis for Powered Lunar Descent and Landing," *The Journal of Spacecraft and Rockets*, Vol. 46, Nov-Dec 2009, pp. 1231–1248.

[30] M. Mitchell, *An Introduction to Genetic Algorithms*. 1996.